ChemPubSoc Europe

DOI: 10.1002/cctc.201800488

CHEMCATCHEM Full Papers

Fabrication of Fe_2C Embedded in Hollow Carbon Spheres: a High-Performance and Stable Catalyst for Fischer-Tropsch Synthesis

Xinsheng Teng,[a] Shouying Huang,*[a] Jian Wang,[a] Hongyu Wang,[a] Qiao Zhao,[a] Yong Yuan,[a] and Xinbin Ma[a]

The Fischer–Tropsch synthesis (FTS) is a non-petroleum-based alternative route, which directly produces fuels and value-added chemicals (e.g. lower olefins) from coal-, biomass- or natural gas-derived syngas. The ε-iron carbide, such as Fe_2C, has been predicted to be active but not stable under high-temperature FTS conditions. In this work, we have fabricated a novel catalyst with Fe_2C embedded in hollow carbon spheres (HCS) by pyrolyzing the coated polymer and $Fe(NO_3)_3$ on silica spheres and then etching the hard template. XRD, XPS, TEM and N_2 physical adsorption were employed to characterize the evolution and properties of as-prepared catalysts, which significantly depend on pyrolysis temperature. Under FTS conditions, the obtained catalysts exhibit good dispersion, robustness of geometric construction, and resistance to sintering. More importantly, Fe_2C was confirmed as the dominant and stable iron carbide species. The unique chemical surrounding and confinement effect provided by carbon matrix contribute to these peculiarities that are responsible for superior activity and stability in FTS. Furthermore, we found that the products distribution could be manipulated by changing the geometric diameters of HCS, due to the tunable CO/H_2 ratio.

Introduction

Fischer–Tropsch synthesis is a flexible and alternative route for production of fuels and key chemicals (e.g. lower olefins) from syngas, which is derived from non-petroleum sources, such as natural gas, coal or biomass.[1,2] Iron-based catalysts have gained much attentions recently, especially in lower olefins production (FTO), due to their low prices, tunable products distribution, high tolerance to operation temperature and broad H_2/CO ratios, and resistance to impurities.[3,4]

Compared with bulk catalysts, supported iron catalysts provide high dispersion of the active species and good mechanical stability.[5–6] Generally, weakly interactive supports (e.g. carbon materials, α-Al_2O_3, SiC) are beneficial to reduction and carburization of iron species, but meanwhile, also to accelerating migration and sintering of iron nanoparticles.

Recently, exploiting carbon materials to disperse and stabilize iron nanoparticles by means of spatial restriction is proposed as a promising strategy to overcome deactivation caused by metal sintering. Bao's group discovered that diffusion and aggregation of the iron species outside carbon nanotubes (CNTs) were unavoidable, while these phenomena could be retarded inside CNTs.[7] Similarly, de Jong and coworkers demonstrated that Fe nanoparticles confined within the internal pore system of ordered mesoporous materials showed resistance to Fe aggregation and carbon fiber formation, resulting in a stable long-term operation for 140 h.[8] In addition, pyrolyzing Fe-based metal organic framework (MOF) can successfully encapsulate Fe phase into a highly porous carbon matrix, which prevents the active carbides from sintering and oxidation.[9–12] Hollow carbon spheres (HCS), as a class of carbon materials with special structure and morphology, are of burgeoning interest in photo-[13] or electro- catalysis,[14] adsorption,[15] drug delivery[16] and so on. Compared with solid counterparts, the nano-sized hollow structure with developed porosity possesses some intrinsic advantages, such as larger exposed surface area on the basis of unit mass, short diffusion path, and fast mass-transfer kinetics.[17] Until now, there are few reports about HCS application in FTS, due to its instability under relatively harsh operation conditions (high temperature and pressure, $>200\,^{\circ}C$, 1 MPa).

On the other hand, iron carbides (e.g. Fe_2C, $Fe_{2.2}C$, Fe_5C_2, and Fe_3C, etc.) detected experimentally are generally accepted as active species in FTS.[1] And their formation, composition and stability relies on many factors such as local chemical environment, crystallite size, morphology and carburization conditions (CO/H_2 ratio, temperature).[18] Among the various iron carbides, ε-Fe_2C, a typical octahedral carbide, is rarely investigated in FTS. Limited to kinetic hindrance and thermodynamic instability, Fe_2C is sporadically identified in both low-temperature and high-temperature FTS. This might result in misunderstanding and misinterpretation about the role of Fe_2C in FTS. Actually, theoretical study has suggested that the barrier of CO dissociation and hydrogenation on Fe_2C is the lowest among the different iron carbides.[19] Zong et al. successfully synthe-

[a] X. Teng, Dr. S. Huang, J. Wang, H. Wang, Q. Zhao, Y. Yuan, Prof. Dr. X. Ma
Key Laboratory for Green Chemical Technology of Ministry of Education
Collaborative Innovation Center of Chemical Science and Engineering,
School of Chemical Engineering and Technology
Tianjin University
Tianjin 300072 (China)
E-mail: huangsy@tju.edu.cn

Supporting information for this article is available on the WWW under https://doi.org/10.1002/cctc.201800488

© 2018 Wiley-VCH Verlag GmbH & Co. KGaA, Weinheim

sized Fe_2C dominant catalysts through carburation of rapidly quenched skeletal iron, which exhibited superior activity in low-temperature FTS, and a linear relationship between activity and amount of Fe_2C has been established.[20] Therefore, fabrication of stable Fe_2C dominant catalyst is promising but challenging in FTS reaction, especially at higher temperature.

Herein, we proposed a protocol to fabricate Fe_2C embedded in HCS catalyst by pyrolyzing polymer and Fe precursor coated on silica spheres and then etching the templates, in which the advantages of Fe_2C and HCS were taken together. Confined within the carbon matrix, nano-sized Fe_2C serves as the dominant iron species and shows good stability during the reaction. The effect of pyrolysis temperature on crystal size, phase and location of iron species as well as texture properties were explored, which significantly influence catalytic performance in FTS. Furthermore, geometric parameter of hollow structure was also manipulated to shed light on the spatial effect of HCS. We found that products selectivity could be tuned, owing to the local CO/H_2 ratios that was dependent on structural peculiarity.

Results and Discussion

Characterization of the as-prepared Fe/HCS

Scheme 1 illustrates the synthetic procedure of the Fe/HCS samples. Briefly, $Fe(NO_3)_3 \cdot 9H_2O$ was impregnated on silica@RF

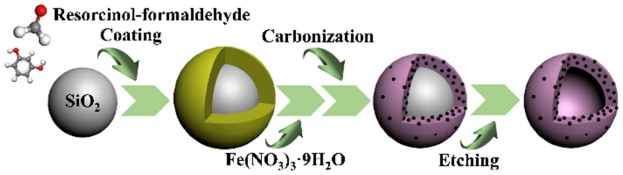

Scheme 1. Schematic illustration of the synthesis of Fe/HCS samples.

spheres followed by pyrolysis and NaOH etching to remove silica spheres. As the SEM images (Supporting Information, Figure S1(a-b)) demonstrates, we obtained the well-dispersed silica spheres with uniform particle sizes by varying the amount of water and TEOS. The average diameters of silica spheres are 150 nm and 260 nm, respectively. After coating carbon precursor, pyrolysis and alkaline etching process, the hollow carbon spheres can be successfully fabricated with different inner diameters but similar wall thickness, depending on the size of the silica sphere template (Supporting Information, Figure S2 (a–b)). We also prepared two reference samples: one is similar to Fe/HCS(150)-600 but without NaOH etching (denoted as Fe/CS(150)-600), the other one is prepared by post-impregnation (denoted as p-Fe/HCS(150)-600). The details are given in experimental section.

Before pyrolysis under N_2 atmosphere, a TG measurement had been performed for the as-prepared Fe/HCS. The ramp rate was 5 °C/min, which was in accordance with that of the actual pyrolysis process. As shown in the TG curve (Supporting information, Figure S3), the weight loss before 200 °C is mainly attributed to be the loss of water. The weight loss before 600 °C is due to the slow decomposition of the polymer. At the same time, the ferric salt precursor decomposes and is reduced. Note that there is an obvious weight loss at 600 °C, stemming from the formation of Fe_xC_y.[21,22] This observation indicates that partial carbon atoms could dissolve into the iron crystal lattice at this temperature, resulting in crystal transformation. Considering the mass loss of carbon layer at different temperature, we varied the concentration of $Fe(NO_3)_3$ solution during impregnation process to keep the Fe loading approximately constant. And the actual Fe loadings obtained from elemental analysis by ICP-OES are listed in Table 1, which are in the range of 17.8~21.5 wt.%. In addition, the content of Na in all the catalyst are less than 0.5 wt.%. Therefore, the influence of Fe loading as well as Na as promoter can be neglected in the following discussion. Moreover, XPS results show that the surface Fe contents of the Fe/HCS samples (Table 1) are much lower than the values from ICP-OES, except for Fe/HCS(150)-500. These differences indicate that an enrichment of Fe species in the bulk take place, owing to the encapsulation of the Fe phase within the carbon matrix.[9,23] These observations are consistent with the TEM images that we present in the following part.

The as-prepared Fe/HCS were obtained after Fe loading and removal of the silica template. Figure 1(a–c) show the TEM images of the as-prepared Fe/HCS(150)-(T) catalysts that were pyrolyzed at different temperatures. Without NaOH etching, the Fe/CS(150)-600 show a core-shell structure with well-dispersed Fe particles (Supporting Information, Figure S4(a)). After etching, it is observed that all the samples possess a well-defined hollow sphere morphology with embedded metal particles. The average diameter of the cavity is about 150 nm, which is similar to that of the silica spheres. The particle size histograms were obtained from TEM analysis using at least 300 Fe nanoparticles,

Table 1. Element content and texture properties of the as-prepared Fe/HCS catalysts.

Catalyst	Fe[a] [wt.%]	Na[a] [wt.%]	Fe surface content[b] [wt.%]	S_{BET}[c] [$m^2 g^{-1}$]	S_{micro}[d] [$m^2 g^{-1}$]	S_{meso}[d] [$m^2 g^{-1}$]	V_{micro}[d] [$cm^3 g^{-1}$]	V_{meso}[e] [$cm^3 g^{-1}$]	$D_{pore,\ average}$[f] [nm]
Fe/HCS(150)-500	21.4	0.4	18.2	388	154	235	0.069	0.334	4.4
Fe/HCS(150)-600	18.1	0.3	11.4	492	206	286	0.094	0.483	5.0
Fe/HCS(150)-700	17.8	0.3	10.7	515	192	325	0.086	0.607	5.6
Fe/HCS(260)-600	21.8	0.4	10.9	545	298	347	0.137	0.452	4.6

[a] Determined by ICP-OES; [b] determined by XPS; [c] calculated according to BET method; [d] calculated according to t-plot method; [e] BJH adsorption cumulative volume of pores between 1.7 nm and 300.0 nm diameter; [f] average pore width calculated according to BET method.

© 2018 Wiley-VCH Verlag GmbH & Co. KGaA, Weinheim

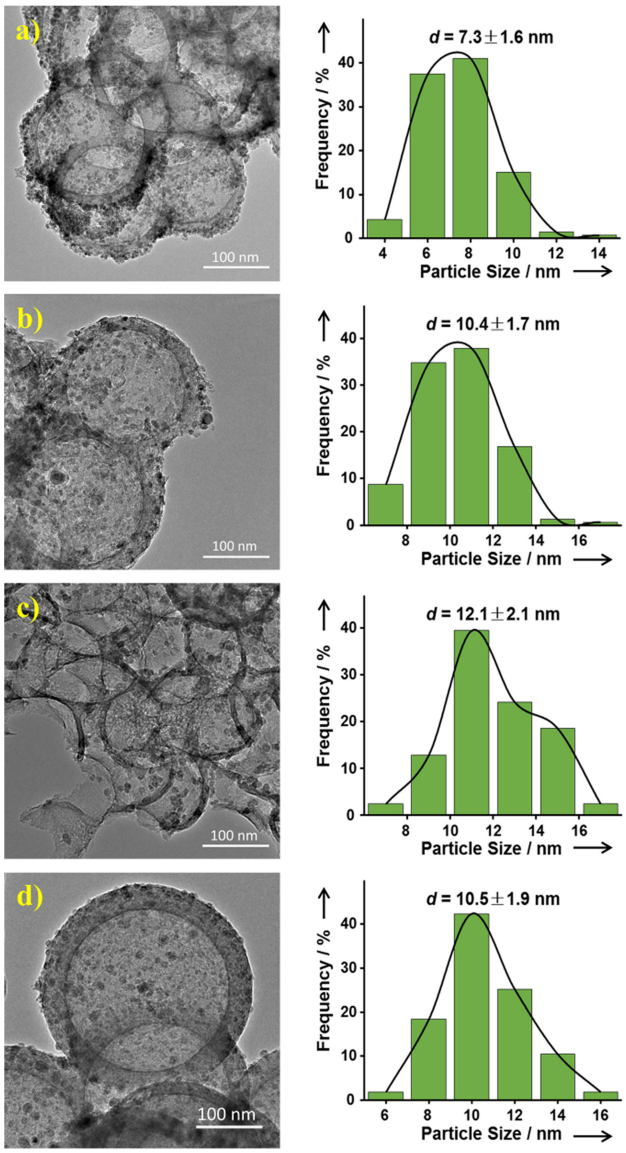

Figure 1. The TEM images of the as-prepared catalysts: a) Fe/HCS(150)-500, b) Fe/HCS(150)-600, c) Fe/HCS(150)-700, d) Fe/HCS(260)-600.

exhibiting normal distribution. Confined within the carbon matrix, the mean size of the Fe particles varies from 7.3 to 12.1 nm with increasing the pyrolysis temperature.[10] In other words, a good dispersion of Fe species can be achieved regardless of the weak interaction between the metal and carbon support. Note that higher temperature also leads to a decreased thickness of the carbon shell, which becomes more pronounced for Fe/HCS(150)-700. Furthermore, partial morphological collapse and distortion can be observed after thermal treatment at 700 °C. Therefore, an appropriate temperature is beneficial to maintain the hollow structure of the samples. When we altered the silica template with a larger size of 260 nm, the diameter of the void could be easily manipulated. As shown in Figure 1(d), the shell thickness and Fe particle size of Fe/HCS(260)-600 are ~30 nm and 10.5 nm respectively, almost the same as those of Fe/HCS(150)-600. It means that pyrolysis temperature is an important factor that significantly affects both the architecture of the hollow catalyst and the dispersion of Fe phase, while the influence of silica sphere could be neglected. For the sample p-Fe/HCS(150)-600, although a hollow structure is also obtained, a large part of iron particles located at external surface of the carbon layer (Supporting Information, Figure S4(c)).

The pore structure of the samples was characterized by N_2 physisorption and the results are summarized in Table 1. All the catalysts provide relatively large specific surface area in the range of 388~545 $m^2 g^{-1}$, which are higher than those of carbon or Al_2O_3 supported iron catalysts.[24–27] As shown in Figure 2(a), the N_2 adsorption-desorption isotherms of the four

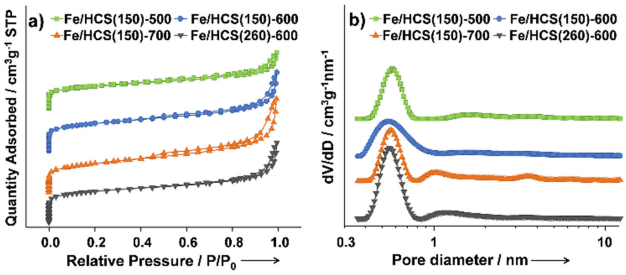

Figure 2. a) N_2 physisorption isotherms and b) pore size distribution of the as-prepared Fe/HCS catalysts.

samples reveal a combination of type I and IV adsorption isotherm characteristic, which indicates the co-existence of micropores and mesopores. The amount of adsorbed N_2 increases linearly at low relative pressure (P/P_0), because of the monolayer adsorption of N_2 on the walls of the micropores. The hysteresis loop at $P/P_0 = 0.35–0.95$ is indicative of mesoporous structure in these samples. Moreover, the hysteresis loop becomes more visible with the increase of the pyrolysis temperature. Correspondingly, the mesoporous surface area gradually increases from 235 $m^2 g^{-1}$ to 325 $m^2 g^{-1}$ accompanied by the increment of BJH adsorption volume from 0.334 $cm^3 g^{-1}$ to 0.607 $cm^3 g^{-1}$, which are mainly responsible for the increase of the total specific surface area and pore volume. These observations demonstrate that the mesoporous structure tends to be formed at higher temperature. Note that the isotherms (Figure 2(a)) exhibit a strong uptake at a high pressure, which may be attributed to the voids formed by the agglomeration of hollow spheres.[28]

The 2D-NLDFT methods was employed to evaluate the pore size distribution in microporous range (Figure 2(b)). It is clear that all the as-prepared catalysts possess pore size at about 0.56 nm, which allows the molecules such as CO, H_2 and lower olefins diffuse into the pores and interact with Fe species. In addition, the larger silica spheres as template results in higher specific surface area and more developed porosity, mainly due to the increased microporosity.

The crystal phase compositions of Fe/HCS catalysts and reference samples were examined by XRD. As shown in Figure 3, there are two main iron phases in Fe/HCS(150)-500, i.e. the diffraction peaks at 35.6°, 57.3° and 62.9°, corresponding to the (311), (511) and (440) facets of hematite (Fe_2O_3, JCPDS

© 2018 Wiley-VCH Verlag GmbH & Co. KGaA, Weinheim

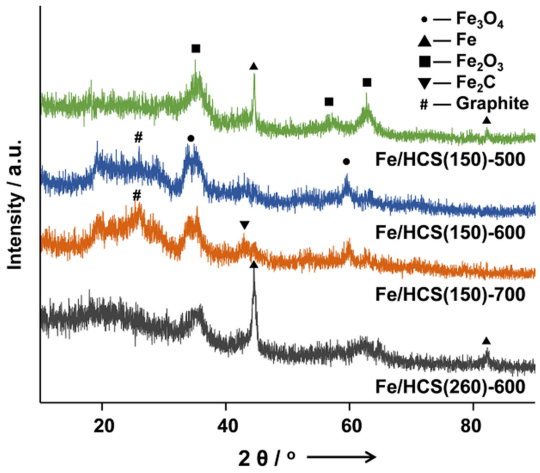

Figure 3. XRD patterns of the as-prepared Fe/HCS catalysts.

39–1346) and the peaks at 44.7° and 82.3°, corresponding to features of metallic Fe (JCPDS 65-4899), respectively. This accords with the existence of satellite peak at 718.9 eV besides the Fe 2p3/2 and 2p1/2 orbital signals in XPS spectrum that is characteristic of Fe_2O_3 (Supporting information, Figure S5).[23] Furthermore, the broad peak emerging around 23° can be assigned to the amorphous structure of the carbon. With increasing the pyrolysis temperature, the reflection at a 2θ value of 26.5° becomes discernible, which is attributed to the characteristic of graphite carbon (JCPDS 65-6212). This indicates the transformation of amorphous carbon into graphite carbon over a Fe-based catalyst at higher temperature, which is in accordance with the previous work.[29] But for the Fe/CS(150)-600 sample, the intense and broad peak of SiO_2 centered at the 2θ range of 17°–32°, making the peak of graphite carbon invisible (Supporting Information, Figure S6(a)). More importantly, the Fe/HCS(150)-600 and Fe/HCS(150)-700 as well as Fe/CS(150)-600 show the dominant phase of magnetite (Fe_3O_4, JCPDS 28-0491), which is different from that of the Fe/HCS (150)-500 sample. Correspondingly, the satellite peak centered at 718.9 eV in XPS almost disappears, indicating the primary species was Fe_3O_4 (Supporting information, Figure S5). Nevertheless, the weak intensity and board FWHM (full width at half maximum) imply the low degree of crystallinity of Fe species.

The calculated crystal size of Fe/HCS(150)-600 and Fe/HCS (150)-700 by Scherrer equation are 6.5 nm and 8.4 nm, respectively, much smaller than the values obtained from TEM images, might due to the existence of a large amount of amorphous Fe species. Moreover, a board peak at 2θ = 42.9° becomes distinguishable for the Fe/HCS(150)-600, Fe/HCS(150)-700 and Fe/CS(150)-600, which is associated with the formation of iron carbide (Fe_2C, JPCDS 17-0897). This phenomenon is consistent with the conclusion derived from TG curve. However, the low intensity also indicates low crystallinity and high dispersion of the Fe_2C species. The XRD pattern of Fe/HCS(260)-600 catalyst is similar to that of Fe/HCS(150)-500 that mainly contains the phase of Fe and Fe_2O_3. Therefore, manipulation of the iron species phases as well as the graphitization degree can be achieved by modifying the pyrolysis conditions and the structural parameter of Fe/HCS. When the Fe precursor is impregnated after pyrolysis procedure (p-Fe/HCS(150)-600), the characteristic peaks of Fe_3O_4 are much more intense, indicating the aggregation and sintering of Fe species without hindrance effect of carbon matrix (Supporting Information, Figure S6(a)).

Raman spectroscopy is a sensitive tool to identify the defects and the degree of graphitization for carbon materials.

As shown in Figure 4, the Raman spectra of all the Fe/HCS catalysts display two distinct peaks at 1337 and 1580 cm^{-1}. The

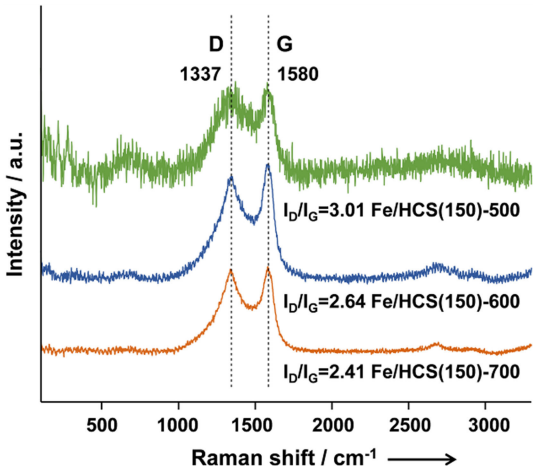

Figure 4. Raman spectra of the as-prepared Fe/HCS catalysts.

peak at 1580 cm^{-1} is assigned to the G band, stemming from the stretching vibration of C=C bond in typical graphitic layers. On the other hand, the D band at 1337 cm^{-1} is a breathing mode of six-fold aromatic rings, representing disordered graphitic carbonaceous species.[30,31] Generally, the ratio of the intensity of D band to G band (I_D/I_G) reveals the defects and disordered degree of carbon atoms. Considering the broadening of the D peak, we fitted the peaks and calculated the area ratio by using Gaussian method.[30] We find that the I_D/I_G ratio decreases as the calcination temperature increases, demonstrating that the graphitization degree is improved by increasing the pyrolysis temperature.

Characterization of the used Fe/HCS Catalysts

After the FTO performance test for 30 h, the fixed bed was cool down to room temperature under argon atmosphere, and then, the catalysts were passivated by a mixture of oxygen (1%) and argon (99%) for further characterization.

As shown in Figure 5, the TEM images of all the used catalysts illustrated that morphology of the hollow spheres is still maintained, indicative of the structural stability under FTS conditions even at high temperature (340 °C). However, sintering of Fe species could be observed with different degree for different catalysts. Several large agglomerates with diameter of 30~40 nm are observed on Fe/HCS(150)-500 and the average particle size rises from 7.3 nm to 16.2 nm. As we mentioned

© 2018 Wiley-VCH Verlag GmbH & Co. KGaA, Weinheim

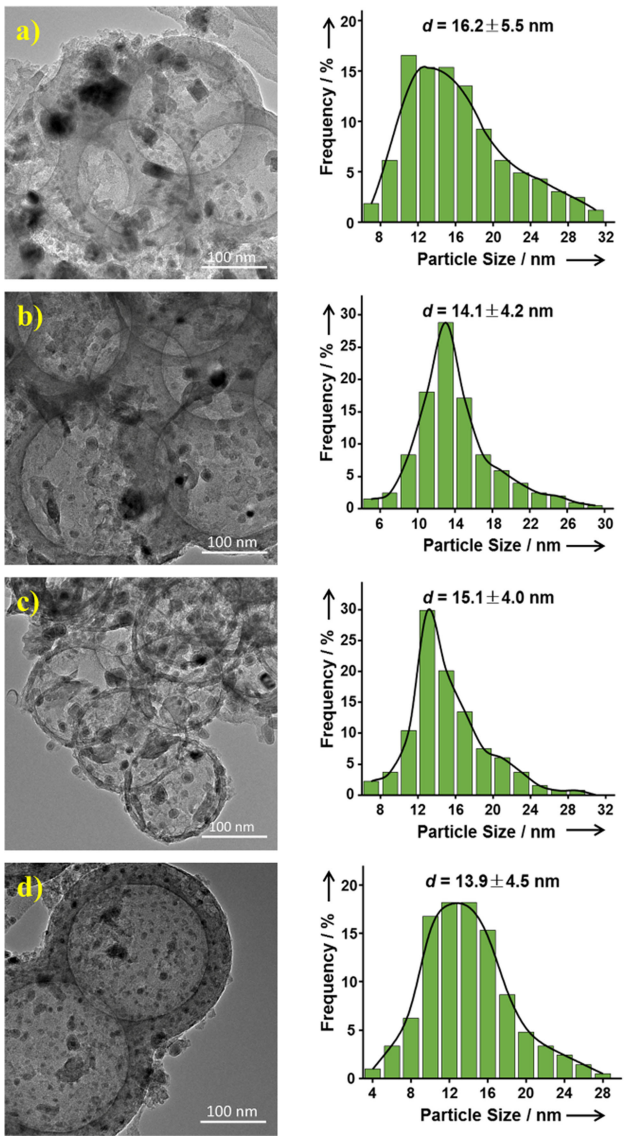

Figure 5. The TEM images of the used catalysts: a) Fe/HCS(150)-500, b) Fe/HCS(150)-600, c) Fe/HCS(150)-700, d) Fe/HCS(260)-600

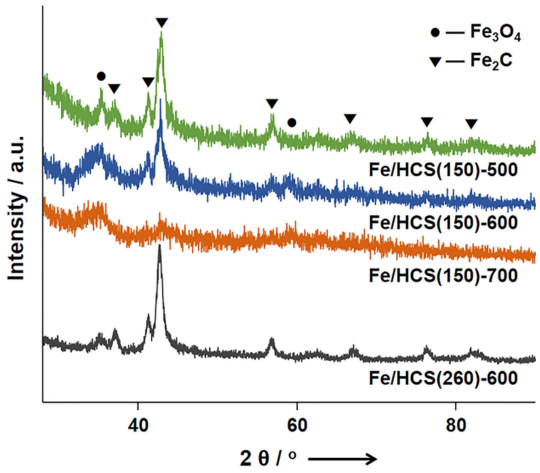

Figure 6. XRD patterns of the used Fe/HCS catalysts

above, XPS and TEM images of as-prepared catalysts reveal that more Fe species are located on the outer surface of hollow spheres for Fe/HCS(150)-500, comparing with other catalysts. Therefore, it is rational that severer agglomeration took place with less constraint effect of carbon matrix. This phenomenon was also observed on the sample of p-Fe/HCS(150)-600 (Supporting Information, Figure S4(d)). In contrast, there is only a slight increase of particle size on the other catalysts, because the encapsulation of Fe species into carbon matrix creates the spatial restriction that prevents their migration and sintering. Hence, we conclude that pyrolysis temperature influences the location as well as distribution of Fe particles within the carbon matrix, which plays an important role in catalytic activity and stability. Moreover, TEM images also illustrate that the Fe nanoparticles evolve into the core-shell-like structure after reaction, due to the formation of Fe carbides and coke deposition under FTO conditions, and the carbonaceous layer outside each particle becomes well-defined gradually with increasing the pyrolysis temperature.

XRD patterns (Figure 6) manifest that all the used catalysts contain Fe_2C (JCPDS 17-0897) as the main Fe phase, which is considered to be active for FTS reaction.[32] It is further validated by the observation of lattice fringes with a spacing of 2.10 Å in TEM images (Supporting Information, Figure S7), which is assigned to the (−101) plane of Fe_2C. In addition, the reflection of Fe_3O_4 phase (JCPDS 28-0491) could be found in the XRD patterns. In most FTS studies, octahedral iron carbides (such as Fe_2C) are sporadically identified after carburization especially in FTO reaction due to their instability at higher reaction temperature.[32] It has been reported that Fe_2C readily evolves into trigonal prismatic (TP) carbides, such as Fe_5C_2.[18] In our case, we note that the Fe_2C phase is the dominant species in the used catalysts. Moreover, the XRD patterns of Fe/HCS(150)-600 obtained at different reaction time (15, 20, 30, 40 h) confirm that the Fe_2C species exist stably without transformation to other carbides (Supporting Information, Figure S8).

According to the literature, the transformation of iron carbides is dependent on many factors, such as crystallite sizes, morphology and surface texture, and the chemical surroundings and so on.[18] The nanocrystalline Fe_2C with smaller size has higher chemical stability because it is more resistant to oxidation by CO_2 and H_2O produced during FTS.[32] This was also confirmed by the sample prepared by post-impregnation. As the crystal size of Fe_3O_4 in p-Fe/HCS(150)-600 is larger than other catalysts, it is reasonable that there are a large proportion of Fe_3O_4 due to oxidation of iron carbides (Supporting Information, Figure S6(b)). On the other hand, the structural and chemical peculiarities of the carbon matrix possibly inhibit the formation of trigonal prismatic carbides from Fe_2C.[18] These factors result in the high robustness of the as-prepared Fe/HCS catalysts. However, it is also noteworthy that the intensity of the characteristic of Fe_2C decreases with increasing pyrolysis temperature. Particularly, the diffraction peaks become very low and broad for Fe/HCS(150)-700, indicating poor crystallinity of Fe phases in this catalyst. The calculated particle sizes of Fe/HCS(150)-500, Fe/HCS(150)-600, Fe/HCS(150)-700 and Fe/HCS

© 2018 Wiley-VCH Verlag GmbH & Co. KGaA, Weinheim

(260)-600 by Scherrer equation are 17.0, 12.4, 7.1 and 14.3 nm, respectively. Compared with the average diameters obtained from the TEM images of the used catalysts, we found that the difference between them becomes more apparent as the pyrolysis temperature increases, possibly stemming from the presence of amorphous and disordered carbides. Note that the (-101) plane of Fe_2C with interplanar spacing of 2.10 Å could be easily observed on Fe/HCS(150)-500 and Fe/HCS(150)-600, while a large amount of amorphous Fe particles without lattice fringes exists in Fe/HCS(150)-700 companied by the presence of Fe_2C and Fe_3O_4 phases (Support information, Figure S7). The observations are consistent with the XRD results. Therefore, the chemical surroundings generated during pyrolysis process is a critical factor that governs the carburization and formation of Fe species.

FTS Performances of the Catalysts

The FTO performance was evaluated at 340 °C, 2 MPa, and a H_2/CO ratio of 1, and the results were summarized in Table 2. The CO conversion with time on stream was plotted in Figure 7. In

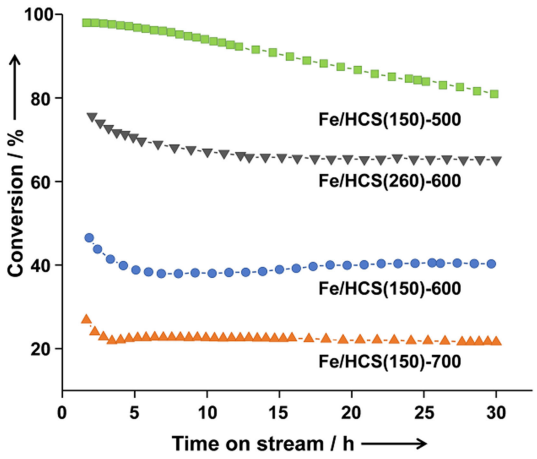

Figure 7. Conversion vs time on stream of the as-prepared Fe/HCS catalysts (340 °C, 2 MPa, GHSV = 27000 mL/(g·h), H_2/CO = 1)

spite of short reduction and activation period (as mentioned in Catalyst Testing), there is no induction period for all the catalysts. It demonstrates that the as-prepared Fe/HCS catalysts are easy to be activated, because the partial carburization could take place during the pyrolysis process. The CO conversion varies from 22.6% to 82.0%, even at a high GHSV of 27000 mL/(g·h). Generally, the initial activity of the catalysts decreases with increasing the pyrolysis temperature from 500 °C to 700 °C, but meanwhile, the deactivation is significantly mitigated. For the Fe/HCS(150)-500, the CO conversion is nearly 96% and declines gradually in 30 h with an almost constant deactivation rate. According to DFT calculations, increasing carbon content weakens the bonding between iron species and CO and hence enhances the FTS activity.[33] Compared with Fe_5C_2 and Fe_3C, Fe_2C as the dominant carbide in Fe/HCS catalysts has the highest carbon content, responsible for the superior activity. It is consistent with the work reported by Zong and coworkers.[20] They attributed the enhanced activity to lower Fe—Fe coordination number at a high content of Fe_2C, which lead to a decrease in dissociation barrier of CO. The migration and sintering of Fe carbides, which are apparent in TEM images, are responsible for the rapid deactivation on Fe/HCS(150)-500. In contrast, Fe/HCS (150)-600 and Fe/HCS(150)-700 show lower activities, stemming from the formation of graphitic carbon that may blocks the accessibility of the active iron species to reactants.[8,18] Besides, Fe/HCS(150)-700 shows the lowest activity with a CO conversion of 22.6%, due to less well-defined Fe_2C phases. This catalyst tends to be stable after a slight decrease at the initial state, which accords with the fact that little sintering is observed in TEM images after reaction (Figure 5(c)). Fe/CS(150)-600 exhibits a comparative activity to Fe/HCS(150)-600, while the p-Fe/HCS(150)-600 shows better but unstable catalytic performance. As most of Fe particles located on external surface for p-Fe/HCS(150)-600, the enhanced activity might be attributed to less diffusion limitation caused by carbon matrix.

The hydrocarbon distributions over these catalysts are shown in Table 2. For the three Fe/HCS(150)-T catalysts, both the selectivity to C_2~C_4 olefins and the O/P ratio increase first and then decrease with increasing the pyrolysis temperature. The Fe/HCS(150)-600 exhibits the best selectivity of lower olefins and highest O/P ratio of 30.1% and 4.8, respectively. The selectivity of CH_4 over Fe/HCS(150)-700 rises to 23.7%, accompanied by an obvious decrease in C_{5+} hydrocarbons. According to the literature, a significant fraction of amorphous iron carbides in Fe/HCS(150)-700 is considered to be responsible for the high selectivity to CH_4.[19]

To investigate the influence of the geometric parameters of hollow carbon spheres on catalytic performance, we synthe-

Table 2. FTO activity and selectivity over the as-prepared Fe/HCS catalysts.[a]

Catalyst	FTY [10^{-6} mol_{CO} g_{Fe}^{-1} s^{-1}]	CO conversion [%]	Selectivity [%]					O/P[b]
			CH_4	C_2~C_4 paraffins	C_2~C_4 olefins	C_{5+}	CO_2	
Fe/HCS(150)-500	628	80.3	16.0	7.8	23.7	49.0	46.4	3.0
Fe/HCS(150)-600	370	40.0	13.3	5.9	28.4	48.5	43.5	4.8
Fe/HCS(150)-700	205	21.8	22.8	13.3	26.2	32.5	32.3	2.0
Fe/HCS(260)-600	495	64.5	23.1	15.2	26.3	32.6	48.3	1.7
Fe/CS(150)-600	402	31.5	34.6	22.2	27.9	13.3	41.2	1.2
p-Fe/HCS(150)-600	475	68.7	31.4	21.8	24.5	20.6	43.3	1.1

[a] Reaction conditions: 340 °C, 2 MPa, GHSV = 27000 mL/(g·h), H_2/CO = 1, the data is collected at time on stream (TOS) = 30 h; [b] The ratio of olefin to paraffin in C_2~C_4 hydrocarbons.

© 2018 Wiley-VCH Verlag GmbH & Co. KGaA, Weinheim

sized Fe/HCS(260)-600 by using the larger silica spheres as templates. The Fe/HCS(260)-600 shows much better activity than that of Fe/HCS(150)-600, and is more stable than Fe/HCS (150)-500 (Figure 7 and Table 2). As we discussed above, the XRD and XPS results manifest that the nature of Fe species in Fe/HCS(260)-600 is similar to Fe/HCS(150)-500 before reaction and the crystallinity of Fe_2C formed during the reaction is higher than other catalysts. Therefore, it is reasonable that Fe/HCS(260)-600 shows a good activity. On the other hand, more Fe species in Fe/HCS(260)-600 are dispersed in carbon matrix not on the outer surface compared with Fe/HCS(150)-500, which could be concluded based on TEM images as well as the element content from XPS. The confinement effect of carbon prevents Fe species form migration and sintering that contributes to the better stability. Comparing the products distribution on Fe/HCS(150)-600 and Fe/HCS(260)-600, we noticed that Fe/HCS(260)-600 shows a higher selectivity of CH_4 with lower selectivity of C_{5+} and O/P ratio. Bao et al. discovered that the concave surface of carbon materials is able to alter the ratio of CO/H_2 by enriching both H_2 and CO molecules, but preferring to CO.[34] And this effect will be enhanced as the curvature of the carbon walls increases, which could tune the reaction rate and product selectivity in CO hydrogenation. In our case, we believe that the enrichment effect of the hollow structure on reactants (CO and H_2) can accelerate the reaction rate. More importantly, the larger the cavity is, the lower ratio CO/H_2 could be observed. Therefore, the promotion effect on secondary hydrogenation is more significant than that on the carbon chain growth, which results in a higher selectivity of alkanes (e.g. CH_4, $C_2 \sim C_4$ paraffins) and lower long chain hydrocarbons and O/P ratio. This conclusion is also strongly supported by the two references (Fe/CS(150)-600 and p-Fe/HCS(150)-600). Without the enrichment effect of hollow structure, the selectivity of CH_4 on the two references is much higher with lower C_{5+} content as well as lower O/P ratio.

Conclusions

In summary, a series of Fe_2C embedded in hollow carbon spheres catalysts have been successfully obtained by using hard template, which showed superior activity and stability in high-temperature FTS. The pyrolysis temperature significantly influenced the nature of Fe species, including phase, particle size and location. Interestingly, we found that the Fe_2C nanocrystalline as the dominant Fe species formed during the reaction and existed stably without transformation to TP carbides (such as Fe_3C and Fe_5C_2) under high-temperature FTS conditions, owing to the specific chemical surroundings by carbon matrix. Moreover, the confinement effects of carbon matrix provided a good dispersion of Fe species and prevented them from migration and agglomeration. These peculiarities of Fe/HCS contributed to the good and stable activity in CO hydrogenation. Furthermore, the product selectivity was tuned by changing inner diameter of the HCS catalysts. As the curvature increased, the selectivity of CH_4 declined with increased O/P ratio, $C_2 \sim C_4$ olefins and C_{5+} hydrocarbons, because of an improved CO/H_2 ratio inside the carbon hollow structure. This work inspires new strategy to adjust and stabilize the phase and particle size of iron carbides and provides a new idea to fabricate carbon nanoreactor with confinement effect that influence not only activity but also product distribution in FTS.

Experimental Section

Materials

Resorcinol, cetyltrimethylammonium bromide (CTAB), tetraethyl orthosilicate (TEOS), ammonia, ethanol, ferric nitrate, and dichloromethane were purchased from Tianjin Kemiou Chemical Reagent Co., Ltd. Formaldehyde was purchased from Beijing J&K Scientific Ltd, and the Sodium hydroxide was obtained from Tianjin Jiangtian Chemical Technology Co., Ltd. All chemicals for catalyst preparation were of analytical grade and were used without any further purification.

Catalyst Preparation

The silica spheres were synthesized by the classical Stöber methods.[35] Typically, 9 mL ammonia aqueous solution was dissolved in a mixture of 16.25 mL ethanol and 70 mL deionized water, stirred at 30 °C for 10 min. Then, a mixture of 10 g TEOS and 45.5 mL ethanol was added to the solution and kept stirring for 1.5 h. The silica spheres were obtained by centrifugation and washed thoroughly with deionized water and ethanol, and then were dried at 70 °C overnight. The particle size of the silica spheres is 150 nm. Changing the amount of deionized water (60 mL) and TEOS (14 g), we obtained the silica spheres with a particle size of 260 nm.

Briefly, 3 g the synthesized silica spheres (150 nm) were dissolved in a mixture of 76.4 mL ethanol and 101.6 mL deionized water with ultrasonic treatment. And then, 1.5 mL ammonia aqueous and 15 mL CTAB solution (0.05 mol/L) were dropwise added into the solution, and then, the obtained mixed solution was stirred for 1 h. Subsequently, 1.35 g resorcinol as the carbon precursor was added into the mixture. After 30 min stirring, 1.89 mL formaldehyde as additional carbon precursor was added. The obtained solution was kept for aging for 24 h at 30 °C under constant stirring and then transferred to a Teflon-lined autoclave and subjected to static hydrothermal synthesis at 100 °C for 24 h. We denoted the silica spheres coated carbon precursor (resorcinol-formaldehyde resin) as silica@RF spheres. The solid product was obtained by filtration and washing with ethanol and deionized water, and finally was dried at 70 °C overnight.

Generally, the catalysts were prepared by excessive impregnation. Briefly, $Fe(NO_3)_3 \cdot 9H_2O$ was dissolved in a mixture of ethanol and CH_2Cl_2. Then, the obtained red solution was used to disperse the silica@RF spheres with the ultrasonic treatment. Afterwards, the suspension was stirred for 12 h at room temperature and then was exposed to the atmosphere for 12 h. The impregnated samples were firstly remove the solvent by rotary evaporation at 40 °C for 1 h and then dried under vacuum at 50 °C overnight. The finally dried product was pyrolyzed at 600 °C under nitrogen for 2 h. After the pyrolysis, the product was washed with NaOH solution (3 mol/L) at 70 °C for 6 h followed by washing with deionized water to remove the silica spheres. Through the above process, the finally catalyst was obtained, denoted as Fe/HCS(150)-T, in which 150 represents the size (nm) of the HCS and T represents the pyrolysis

© 2018 Wiley-VCH Verlag GmbH & Co. KGaA, Weinheim

temperature (°C). For comparison, the catalyst Fe/CS-600 was prepared as Fe/HCS(150)-600 without etching the silica. Besides, a catalyst prepared by post-impregnation (denoted as p-Fe/HCS (150)-600) was also investigated as a reference sample. The silica@RF spheres were firstly calcinated at 600 °C, and then impregnate $Fe(NO_3)_3{\cdot}9H_2O$ followed by removal of the silica template. At last, another calcination was performed to decompose Fe precursor.

To explore the effect of geometric structure, we prepared a catalyst by using the silica spheres of 260 nm as template for comparison. After dispersing the silica spheres with the average diameter of 260 nm in a mixture of ethanol and deionized water, we added 1.2 mL ammonia aqueous and 15 mL CTAB solution (0.04 mol/L) into the solution. Then 1.08 g resorcinol and 1.5 mL formaldehyde were added as carbon precursors, and the rest of the procedure is the same as the above. The obtained product was pyrolyzed at 600 °C under N_2 flowing, followed by removing the silica spheres template. The as-prepared catalyst was named as Fe/HCS(260)-600.

Catalyst Characterization

To verify the crystal structure of the catalysts, the powder X-ray diffraction (XRD) was performed on a RigakuD/max-2500 diffractometer with a CuKα radiation (λ = 1.5406 Å). The patterns were collected at 40 kV and 200 mA with scan speed of 8°/min. The morphology and microstructure of the samples were measured by the Tecnai G2 F20 transmission electron microscope (TEM) at 200 kV and the S-4800 scanning electron microscope (SEM). The samples were dispersed in ethanol with ultrasound-assistance and then dripped onto a micro-grid and a small piece of silica glass, respectively. The Raman spectra was collected at room temperature on DXR Microscope (Renishaw, InVia reflex) with spectral resolution of 1.496 cm^{-1}. A 532 nm^{-1} diode-pump solid semiconductor laser was used as the excitation source with the power output of 80 mW. The scanning wavenumber was ranged from 50 cm^{-1} ~ 3500 cm^{-1}. Thermogravimetric (TG) analysis was performed on a thermogravimetric analyzer (STA449F3, NETZSCH Corp.). The sample was heated from 40 °C to 800 °C in nitrogen atmosphere (80 mL/min) with a heating rate of 5 °C/min. The surface area and pore structure were determined by Micromeritics ASAP-2020 analyzer instrument at −196 °C. Prior to measurement, the samples were degassed at 200 °C for 6 h. The specific surface area (S_{BET}) was calculated by using the Brunauer–Emmett–Teller (BET) method. The micropore surface area (S_{micro}) and total micropore volume (V_{micro}) were determined by t-plot method, and the pore size distributions was obtained by the 2D-NLDFT method. The Inductively-Coupled-Plasma Optical Emission Spectroscopy (ICP-OES, Vista-MPX) was employed to determine the elemental loading. Before the test, the sample was dissolved in a 1:1.2:7.2 mixture of HF: HNO_3 (65%): HCl (35%) solution by using the Microwave Reaction System (Anton Paar, Multiwave 3000). The samples' X-ray photoelectron spectra (XPS) were recorded on a Thermo Fisher ESCALAB 250Xi K-Alpha equipment which was using the Al–Kα (1486.8 eV) as the excitation source. The XPS spectra were taking the spectrum of C 1s at 284.8 eV as an internal standard.

Catalyst Testing

FTO experiments were performed using a tubular fix-bed reactor. For each run, 200 mg of catalyst with the particle size of 700 ~ 1700 μm was diluted with 2300 mg quartz sand and then placed into a stainless-steel reactor tube (inner diameters of 8.0 mm). Prior to reaction, the as-prepared catalyst was in-situ reduced at 350 °C (10 °C/min), 0.1 MPa for 2 h in pure H_2 flow, then the temperature of catalyst bed was cooled down to 290 °C. Subsequently, the syngas mixture (H_2/CO = 1) with GHSV = 27000 mL/(g·h) was introduced to activate the catalysts for 1 h. After all the pretreatment, the reaction was carried out at 340 °C with the pressure of 2 MPa and H_2/CO ratio is 1. The heavy hydrocarbons (C_{5+}) were separated and collected by using a hot trap at 135 °C between reactor and back pressure regulator. The uncondensed product stream was analyzed by using an on-line gas chromatograph (Agilent GC 7890B) equipped with two thermal conductivity detectors (TCD) and one flame ionization detector (FID). The catalytic activity was presented by the molar conversion of CO per gram of iron per second (FTY). The selectivities to hydrocarbons were determined on the carbon basis except CO_2.

Acknowledgements

Financial support from the National Natural Science Foundation of China (U1462204, 21325626 and 21506154), Natural Science Foundation of Tianjin City (18JCQNJC05900) and the Program of Introducing Talents of Discipline to Universities (B06006) is gratefully acknowledged.

Conflict of Interest

The authors declare no conflict of interest.

Keywords: Fischer-Tropsch synthesis · Hollow carbon sphere · Fe_2C · Pyrolysis

[1] H. M. T. Galvis, K. P. de Jong, *ACS Catal.* **2013**, *3*, 2130–2149.
[2] E. de Smit, B. M. Weckhuysen, *Chem. Soc. Rev.* **2008**, *37*, 2758–2781.
[3] Y. Yuan, S. Huang, H. Wang, Y. Wang, J. Wang, J. Lv, Z. Li, X. Ma, *ChemCatChem* **2017**, *9*, 3144–3152.
[4] Y. Cheng, J. Lin, K. Xu, H. Wang, X. Yao, Y. Pei, S. Yan, M. Qiao, B. Zong, *ACS Catal.* **2016**, 6, 389–399.
[5] H. M. T. Galvis, J. H. Bitter, C. B. Khare, M. Ruitenbeek, A. I. Dugulan, K. P. de Jong, *Science* **2012**, *335*, 835–838.
[6] F. Jiang, M. Zhang, B. Liu, Y. Xu and X. Liu, *Catal. Sci. Technol.* **2017**, *7*, 1245–1265.
[7] W. Chen, Z. Fan, X. Pan, X. Bao, *J. Am. Chem. Soc.* **2008**, *130*, 9414–9419.
[8] M. Oschatz, T. W. van Deelen, J. L. Weber, W. S. Lamme, G. Wang, B. Goderis, O. Verkinderen, A. I. Dugulan, K. P. de Jong, *Catal. Sci. Technol.* **2016**, *6*, 8464–8473.
[9] V. P. Santos, T. A. Wezendonk, J. J. Jaen, A. I. Dugulan, M. A. Nasalevich, H. U. Islam, A. Chojecki, S. Sartipi, X. Sun, A. A. Hakeem, A. C. Koeken, M. Ruitenbeek, T. Davidian, G. R. Meima, G. Sankar, F. Kapteijn, M. Makkee, J. Gascon, *Nat. Commun.* **2015**, *6*, 6451.
[10] T. A. Wezendonk, V. P. Santos, M. A. Nasalevich, Q. S. E. Warringa, A. I. Dugulan, A. Chojecki, A. C. J. Koeken, M. Ruitenbeek, G. Meima, H.-U. Islam, G. Sankar, M. Makkee, F. Kapteijn, J. Gascon, *ACS Catal.* **2016**, *6*, 3236–3247.
[11] B. An, K. Cheng, C. Wang, Y. Wang, W. Lin, *ACS Catal.* **2016**, *6*, 3610–3618.
[12] S. Y. Hong, D. H. Chun, J. I. Yang, H. Jung, H. T. Lee, S. Hong, S. Jang, J. T. Lim, C. S. Kim, J. C. Park, *Nanoscale* **2015**, *7*, 16616–16620.
[13] C. Liu, Z. Chen, Z. Wang, W. Li, E. Ju, Z. Yan, Z. Liu, J. Ren, X. Qu, *Nanoscale* **2016**, *8*, 12570–12578.
[14] Q. Gao, Q. Lai, Y. Liang, *RSC Adv.* **2015**, *5*, 103302–103307.
[15] D. Liu, Y. Guo, L. Zhang, W. Li, T. Sun, A. Lu, *Small* **2013**, *9*, 3852–3857.
[16] H. Wang, X. Li, Z. Ma, D. Wang, L. Wang, J. Zhan, L. She, F. Yang, Int. J. *Nanomedicine* **2016**, *11*, 1793–1806.
[17] X. Xu, F. Nosheen, X. Wang, *Chem. Mater.* **2016**, 28, 6313 − 6320.
[18] E. de Smit, F. Cinquini, A. M. Beale, O. V. Safonova, W. van Beek, P. Sautet, B. M. Weckhuysen, *J. Am. Chem. Soc.* **2010**, *132*, 14928–14941.

© 2018 Wiley-VCH Verlag GmbH & Co. KGaA, Weinheim

[19] C. Huo, Y. Li, J. Wang, H. Jiao, *J. Am. Chem. Soc.* **2009**, *131*, 14713–14721.
[20] K. Xu, Y. Cheng, J. Lin, H. Wang, S. Xie, Y. Pei, S. Yan, M. Qiao, Z. Li, B. Zong, *J. Catal.* **2016**, *339*, 102–110.
[21] S. Ren, R. Prakash, D. Wang, V. S. Chakravadhanula, M. Fichtner, *ChemSusChem* **2012**, *5*, 1397–1400.
[22] R. Prakash, A. K. Mishra, A. Roth, C. Kübel, T. Scherer, M. Ghafari, H. Hahn, M. Fichtner, *J. Mater. Chem.* **2010**, 20, 1871.
[23] Q. Chen, G. Liu, S. Ding, M. C. Sheikh, D. Long, Y. Yoneyama, N. Tsubaki, *Chem. Eng. J.* **2018**, *334*, 714–724.
[24] K. Keyvanloo, W. C. Hecker, B. F. Woodfield, C. H. Bartholomew, *J. Catal.* **2014**, *319*, 220–231.
[25] H. Xiong, M. Moyo, M. A. Motchelaho, Z. N. Tetana, S. M. A. Dube, L. L. Jewell, N. J. Coville, *J. Catal.* **2014**, *311*, 80–87.
[26] R. M. M. Abbaslou, A. Tavassoli, J. Soltan, A. K. Dalai, *Appl. Catal. A* 2009, 367, 47–52.
[27] G. Yu, B. Sun, Y. Pei, S. Xie, S. Yan, M. Qiao, K. Fan, X. Zhang, B. Zong, *J. Am. Chem. Soc.* 2010, 132, 935–937.
[28] Y. Sang, Q. Jiao, H. Li, Q. Wu, Y. Zhao, K. Sun, *J. Nanopart. Res.* **2014**, *16*, 2755.
[29] R. Qiang, Y. Du, H. Zhao, Y. Wang, C. Tian, Z. Li, X. Han, P. Xu, *J. Mater. Chem. A* **2015**, *3*, 13426–13434.
[30] A. C. Ferrari, J. Robertson, *Phys. Rev. B* **2000**, *60*, 14095–14107.
[31] B. Yan, S. Huang, S. Wang, X. Ma, *ChemCatChem* **2014**, *6*, 2671–2679.
[32] K. Xu, B. Sun, J. Lin, W. Wen, Y. Pei, S. Yan, M. Qiao, X. Zhang, B. Zong, *Nat. Commun.* **2014**, *5*, 5783.
[33] J. Cheng, P. Hu, P. Ellis, S. French, G. Kelly, C. M. Lok, *J. Phys. Chem. C* **2009**, *114*, 1085–1093.
[34] J. Guan, X. Pan, X. Liu, X. Bao, *J. Phys. Chem. C* **2009**, *113*, 21687–21692.
[35] W. Stöber, A. Fink, E. Bohn, *J. Colloid Interface Sci.* **1968**, *26*, 62–69.

Manuscript received: March 23, 2018
Accepted Article published: June 21, 2018
Version of record online: July 19, 2018

© 2018 Wiley-VCH Verlag GmbH & Co. KGaA, Weinheim